Friction

Research Article

Scratch-induced damage of doped DLC and MoS_2 coatings—Deep symbolic analysis

Ming Liu[1,2,†], Zhitong Xu[2,†], Noraphat Yuktanan[3], Tang Gu[3,✉], Guangan Zhang[4,5,6,✉], Jinyang Jiang[7,8], Fuqian Yang[9,✉], Rui Liang[1,✉]

Cite this article: Liu M, Xu ZT, Yuktanan N, et al. *Friction* 2026, **14**(3): 9441166. https://doi.org/10.26599/FRICT.2025.9441166

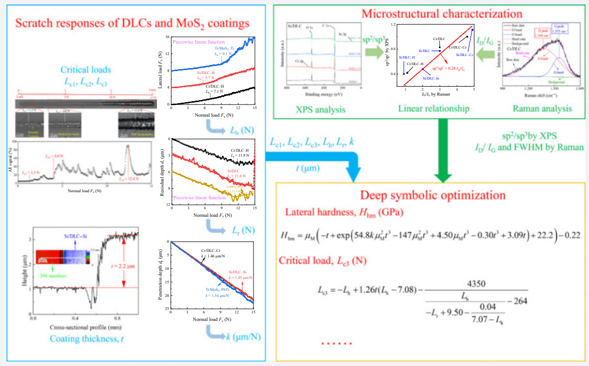

ABSTRACT: Understanding contact-induced damage is of paramount importance in the analysis of the lifespan and performance of surface coatings. In this work, we investigate the effects of dopants and interlayers on the structural durability of diamond-like carbon coatings (DLCs) and molybdenum disulfide (MoS_2) coatings on stainless steel via microscratch tests. The analysis of X-ray photoelectron spectroscopy (XPS) survey spectra and Raman spectra of the DLCs shows that the ratio of sp^2/sp^3 (i.e., the intensity ratio of sp^2 to sp^3 obtained via XPS) is proportional to I_D/I_G, where I_D and I_G are the intensities of the D and G bands of the Raman spectrum, respectively. The analysis of the scratch tests reveals that there are three critical loads for the scratch-induced damage of the DLCs and MoS_2 coatings, corresponding, respectively, to the initiation of periodic V-cracking, the minimum load for periodic semicircle cracking or peel-off, and the minimum load for partial and periodic delamination. Dopants can reduce the friction coefficient of DLCs and have a negligible effect on Ti/MoS_2 coatings. The Cr interlayer can better enhance the bonding strength between the DLCs and the steel substrate than the Si interlayer. Doping Cr and H can reduce the hardness of DLCs; doping Si can increase the hardness of DLCs; doping Ti, Pb, and PbTi can reduce the hardness of MoS_2 coatings. The deep symbolic optimization (DSO) algorithm is used to establish nominal-mathematical formulations between the critical variables for the scratch test and the material parameters of the surface coating. The DSO analysis demonstrates the feasibility of using "deep learning" to establish "quantitative" relationships between the critical variables for mechanical deformation and material parameters.

KEYWORDS: microscratch; diamond-like carbon coating (DLC); MoS_2 coating; deep symbolic optimization (DSO) algorithm

1 Introduction

AISI 304 stainless steel is a widely utilized material in medical, aerospace, automotive, military, oil, and gas applications [1]. However, its low hardness, high friction coefficient, and low corrosion resistance limit its wide application. To overcome these disadvantages and reduce the damages from fretting wear and contact fatigue to AISI 304 stainless steel, protective coatings with high performance [2] (e.g., excellent corrosion resistance [3, 4], high-temperature oxidation resistance [5], excellent lubrication properties [6], remarkable antifogging and defogging abilities [7], high-temperature conductivity [8], and excellent thermal performance [9]), such as diamond-like carbon coatings (DLCs) and molybdenum disulfide (MoS_2) coatings, have been investigated. DLCs offer high hardness, excellent corrosion resistance, and low friction, while MoS_2 coatings provide low friction, good thermal and chemical stability, and high mechanical strength [10–12].

† Ming Liu and Zhitong Xu contributed equally to this work.

[1] Department of Engineering Science, Faculty of Innovation Engineering, Macau University of Science and Technology, Macau 999078, China. [2] Fujian Provincial Key Laboratory of Terahertz Functional Devices and Intelligent Sensing, School of Mechanical Engineering and Automation, Fuzhou University, Fuzhou 350108, China. [3] DR2I, Institute of Polytechnic Science and Aeronautics (IPSA), Ivry-Sur-Seine 94200, France. [4] State Key Laboratory of Solid Lubrication, Lanzhou Institute of Chemical Physics, Chinese Academy of Sciences, Lanzhou 730000, China. [5] Institute of Nanomaterials Application Technology, Gansu Academy of Science, Lanzhou 730000, China. [6] Center of Materials Science and Optoelectronics Engineering, University of Chinese Academy of Sciences, Beijing 100049, China. [7] State Key Laboratory of Engineering Materials for Major Infrastructure, School of Materials Science and Engineering, Southeast University, Nanjing 211189, China. [8] Jiangsu Key Laboratory for Construction Materials, School of Materials Science and Engineering, Southeast University, Nanjing 211189, China. [9] Materials Program, Department of Chemical and Materials Engineering, University of Kentucky, Lexington, KY 40506, USA.

✉ Corresponding authors. E-mail: T. Gu, tang.gu@ipsa.fr; G. Zhang, gazhang@licp.cas.cn; F. Yang, fyang2@uky.edu; R. Liang, rliang@must.edu.mo

Received: March 4, 2025; Revised: May 22, 2025; Accepted: August 4, 2025

Nomenclature

A_{1g}	Peak associated with the out-of-plane vibrations of S atoms	n	Number of data points
d_p	Penetration depth	S_a	Area arithmetical mean height
d_r	Residual depth	S_h	Horizontally projected contact area
d_t	Sphere-to-cone transition depth of Rockwell C indenter	sp^2/sp^3	Intensity ratio of sp^2 over sp^3 by analyzing X-ray photoelectron spectroscopy (XPS) spectra
$\mathbf{E}^1_{2g}$	Peak associated with in-plane vibrations of Mo and S atoms	S_q	Area root mean square roughness
f	Symbol of mathematical function	S_n	Vertically projected contact area
F_n	Applied normally load	$p(\tau\|\gamma)$	Distribution of mathematical expressions
F_h	Measured lateral (or tangential) force	X	Input variables
H_h	Lateral scratch hardness	X_i	i-th input variable
H_n	Normal scratch hardness	y	Output variable
H_{nm}	Mean value of H_n for $F_n > L_{c3}$	y_i	i-th output variable
H_{hm}	Mean value of H_h for $F_n > L_{c3}$	λ	Wavelength of X-ray (Cu Kα)
I_D/I_G	Intensity ratio of D and G bands by analyzing Raman spectra	θ	Half-apex angle of Rockwell C indenter
$J(\gamma;\varepsilon)$	Learning objective	μ	Scratch friction coefficient
k	Proportional coefficient of d_p vs. F_n	μ_M	Mean value of μ for $F_n < L_{c1}$
L_{c1}	Minimum load for the initiation of periodic V-cracks	σ	Standard deviation of the target values
L_{c2}	Minimum load for the occurrence of periodic semicircle cracks for the Cr/DLC and Cr/DLC–Cr coating and peel-off for other coatings	τ	Sampled expression
L_{c3}	Minimum load at which partial and periodic (P&P) delamination occurs	γ	The parameter of RNN
L_h	Transition of the piecewise linear function for F_h vs. F_n	ω_D	Wavenumber of D peak
L_r	Transition of the piecewise linear function for d_r vs. F_n	ω_G	Wavenumber of G peak

The rapid development of technology and industry has stimulated interest in the development of composite coatings with dopants, which can improve the bonding strength and functions under complex service environments. There are reports on the doping of metallic or nonmetallic elements to improve the performance of DLCs and MoS_2 coatings. Liu et al. [13] reported that adding H to DLCs led to an increase in hardness and a decrease in resistance to cracking failure, and adding Si or Cr increased fracture toughness. Su et al. [14] and Kim et al. [15] reported that doping with Mo and Ti, respectively, significantly enhanced the tribological performance of DLCs. Yetim et al. [16] demonstrated that the reaction of metallic elements (e.g., Ti, Al, and V) with carbon improved the bonding between DLCs and substrates and the tribological performance of DLCs. Gao et al. [17] reported that the addition of carbon fiber–graphene oxide (CF–GO) can improve the wear resistance of MoS_2 coatings. Su and Kao [18] reported that Cr doping can increase the tribological performance of MoS_2.

The scratch technique is a useful tool for assessing the tribological behavior of a solid surface [19, 20] and the adhesion/bonding strength between the surface coating and the substrate. Liu and Yan [21] studied the deformation and cracking of doped DLCs during Vickers scratching under a progressive normal load. Segura-Giraldo et al. [22] reported an increase in the bonding strength between DLCs and 316 steel substrates with TiN interlayers. Wang et al. [23] evaluated the effect of the a-Si:H interlayer on the bonding of DLCs and Fe-based substrates and pointed to the contribution of the formed Si–Fe to the bonding strength. Conducting thermomechanical scratching on an atomic force microscope, Chang et al. [24] observed nanoexfoliation and morphological changes in multilayer MoS_2. Kim and Ahn [25] investigated the nanotribological behavior of a MoS_2 bilayer on a SiO_2/Si substrate and revealed the sequential degradation of the MoS_2 bilayer from the top layer to the bottom layer. Renevier et al. [26] examined the effects of metallic doping (Cr, W, and Zr) on the tribological behavior of MoS_2/Ti coatings. They reported that MoS_2/metal coatings were harder than pure MoS_2 coatings. Stoyanov et al. [27] studied the size-dependent tribological behavior of Ti–MoS_2. All these studies highlight the complexity of the scratching deformation of surface coatings and multilayer structures. The scratching responses of DLCs and MoS_2 coatings remain elusive.

Deep learning-based approaches have shown enormous potential for quantitatively analyzing complex phenomena (e.g., the driving forces for material failure or fatigue [28–31] and the effects of hydrogen and temperature [32–34]). It has been used to evaluate the effects of plastic deformation on the scratching responses of metallic materials [35, 36], glass [37], and ceramic coatings [38] with excellent predictability.

Symbolic regression (SR), which evolved from genetic programming (GP) [39, 40], has been used to establish mathematical expressions from experimental data. The SR principle rests on recombination and mutation with neural-guided GP population seeding [41]. Schmidt and Lipson [42] applied SR to determine free-form natural laws from experimental data. Brunton et al. [43] demonstrated the application of SR to a dynamical system with governing equations derived from data through sparse identification. Petersen et al. [44] and Landajuela et al. [45] proposed deep symbolic regression (DSR), in which a recurrent neural network is trained via a risk-seeking policy gradient to generate candidate expressions. Lu et al. [46] introduced the deep differentiable SR neural network (DDSR-NN), a neural network with layers representing continuous distributions over mathematical operators, allowing for gradient-based optimization. The deep symbolic optimization (DSO) algorithm is a deep learning framework for symbolic optimization tasks based on SR, DSR, and DDSR-NN [47]. Currently, few studies have focused on the use of deep learning-based approaches to analyze the scratching behavior of DLCs and MoS_2 coatings, which are likely to exhibit distinct scratching damage.

This work aims to investigate the scratch-induced damage of DLCs and MoS_2 coatings with a focus on the influence of different interlayers (i.e., Cr, Si, and Ti) and dopants (i.e., Cr, H, Si, Ti, and Pb). A Rockwell C 120° diamond indenter was used in the scratch tests under a ramping load. Both the normal and tangential hardness values were calculated and compared. Notably, the scratch responses of DLCs are different from those of MoS_2 coatings, e.g., DLCs have higher acoustic emission (AE) than MoS_2 coatings under larger loading. DSO, which was used to modify crack tip formulas and capture the Mullins effect in elastomers from finite element simulations [48] and temperature-dependent benchmark tests [49], was used to quantify the dependences of the scratching responses on the thickness and material parameters of the coatings.

2 Experimental

2.1 Preparation and characterization of DLCs and MoS_2 coatings

AISI 304 stainless steel films with a 1 mm thick square shape (30 mm × 30 mm) were used as the substrates for the DLCs and MoS_2 coatings. The steel films were sequentially cleaned in petroleum ether and alcohol for 20 min, ultrasonicated and then blow-dried with nitrogen. DLCs with different dopants (e.g., Si, Cr, H) and Si or Cr interlayers and MoS_2 coatings with Ti interlayers and different dopants (i.e., Ti, Pb, and PbTi) were deposited over the prepared steel films on a UDP650 system (Teer Coatings Ltd., UK) equipped with various targets (i.e., C, Cr, Si, Ti, and Pb with 99.99% purity and MoS_2 with 99.95% purity). The deposition parameters of the DLCs and MoS_2 coatings are listed in Table 1. A confocal microscope (Olympus LEXT OLS5100, Japan) was used to measure the thicknesses of the coatings. The thickness of the coatings is ~2 μm, as measured by a confocal microscope. Prior to the measurement, the confocal microscope was calibrated on a standard glass sample with a step size of 2 μm. Multiple measurements were conducted at different regions across the step on the standard sample to ensure good consistency and high precision in the measurement of the coating thickness. The measurements were conducted in a clean room with constant temperature and humidity to minimize the environmental impact. See Fig. S1 in the Electronic Supplementary Material (ESM) for the determination of the coating thickness. The coating thickness t and corresponding numerical values of area-arithmetical mean height (S_a) and area root mean square roughness (S_q) for randomly selected surface areas are also listed in Table 1.

The microstructures of the as-deposited DLCs and MoS_2 coatings were determined via X-ray diffraction (XRD) on an X-ray diffractometer (DY1602, Empyrean, UK) with Cu Kα ray of λ = 0.1542 nm under a tube voltage of 45 kV and a tube current of 40 mA. Raman spectroscopy was performed to analyze the microstructural characteristics of the DLCs under an excitation wavelength of 532 nm via an InVia Reflex Raman Microscope (Renishaw, Wotton-Under-Edge, UK) with WiRE™ 4.2 software (Renishaw, UK). X-ray photoelectron spectroscopy (XPS) was conducted to investigate the chemical states of the DLCs and MoS_2 coatings on an ESCALAB-250 (Thermo Fisher, USA) instrument under monochromatized Al Kα-line radiation.

2.2 Microscratch tests of the coatings

Microscratch tests were performed on a microscratch tester (MST², Anton Paar, Austria) equipped with an AE detector in the air at 23 °C. A Rockwell C 120° diamond indenter was used in the tests under a load range of 5 mN–15 N, and the relative humidity was 45% during the testing. The scratch length l was ~3 mm, and the applied load F_n linearly increased from 5 mN to 15 N to comprehensively evaluate the distinct failure modes, the transition from coating-dominated to system-dominated behavior, and the mechanical responses of the coating and the coating/substrate system. Several factors were considered in determining the use of 15 N: The load range (5 mN–15 N) allowed for a systematic investigation of both the intrinsic properties (e.g., hardness and cohesion strength) of the coating and the scratch behavior of the coating/substrate system under progressively increasing loads. Smaller loads help to limit the contribution of the substrate, whereas higher loads can introduce the contribution of the substrate and induce damage at the coating/substrate interface. This makes it possible to determine critical parameters such as bonding strength. The load of 15 N is high enough to induce plastic deformation of the steel substrate and delamination of the coatings. Thus, no loads higher than 15 N were used in the scratch tests. Note that a film/substrate structure can experience rapid changes in response mode under a large normal load during a scratch test, which can obscure the coating-specific characteristics and accelerate damage evolution, resulting in large scatterings of critical parameters, such as critical loads.

Figure 1 shows a schematic of the scratching test with a Rockwell C diamond indenter of a half-apex angle θ of 60° and a spherical tip radius R of 108 μm, which can be validated by scanning electron microscopy [50], under a progressive normal load. The sphere-to-cone transition depth d_t (= $R(1-\sin\theta)$) is calculated to be 14.5 μm. The Rockwell C indenter is widely

Table 1 Deposition parameters, thickness t, and area roughness of DLCs and MoS_2 coatings

Interlayer	Coating	Target current (A)		Butane (cm^3/min)	t (μm)	S_a (μm)	S_q (μm)
		Si/Cr	Pb/Ti				
Cr	DLC	—		—	2.0	0.150	0.221
	DLC–Cr	/0.38	—		1.9	0.190	0.332
	DLC–H	—		16	3.0	0.300	0.420
Si	DLC	—			2.1	0.053	0.089
	DLC–Si	0.5/		—	2.2	0.101	0.164
	DLC–Cr	/0.3	—		1.8	0.086	0.136
	DLC–H	—		16	2.5	0.096	0.157
Ti	MoS_2		—		2.0	0.097	0.131
	MoS_2–Ti		/0.4		1.3	0.054	0.083
	MoS_2–Pb	—	0.2/	—	1.4	0.072	0.134
	MoS_2–PbTi		0.2/0.4		1.4	0.046	0.086

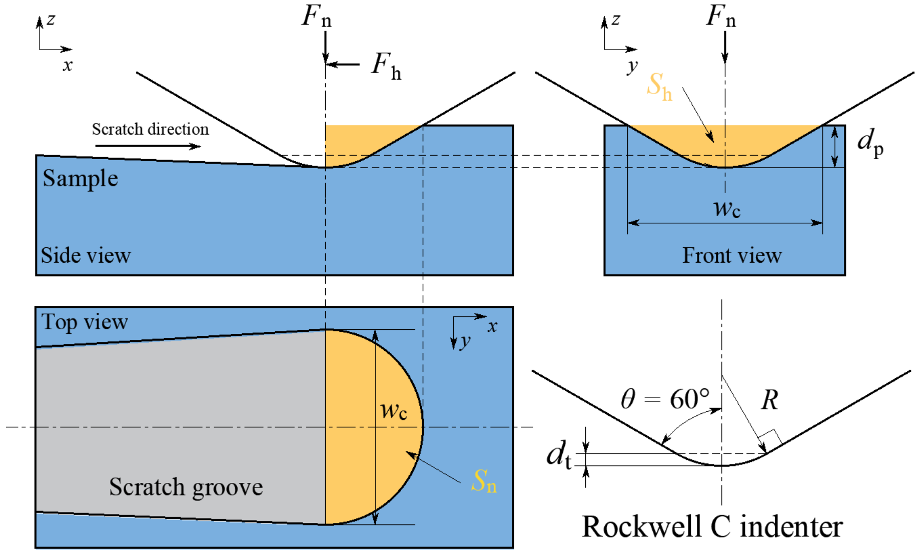

Fig. 1 Schematic of scratching by a Rockwell C 120° indenter with a half-apex angle of 60° under a progressive load (w_c is the vertically projected contact width).

utilized in the failure analysis of coatings [51, 52], and is more suitable for studying damage evolution with the transition from cracking to delamination than sharp indenters, such as the Berkovich indenter [50] and the Vickers indenter [21], since scratches with a Rockwell C indenter can produce deformation and progressive damage as the applied normal load increases.

Each scratch test consisted of three steps. (1) Prescan under an extremely small normal load of 5 mN before normal scratching to measure the initial surface profile, which was set as the baseline. Its effect on scratching deformation is negligible [53]. (2) Normal scratching with the indenter on the sample surface at a constant speed of 6 mm/min (low enough to minimize thermal effects during scratching) for a total scratch length of l = 3 mm in 30 s. The normal load increased linearly from 5 mN to 15 N. (3) A panoramic image of the residual scratch groove was captured under a normal load of 5 mN after normal scratching to measure the residual depth along the scratch track. Both true penetration depths and residual depths were derived from the surface inclination and the subtraction of the normal displacements of the scratch test and the postscan from the initial surface height (i.e., the displacement data obtained during the prescan), respectively.

The scratch friction coefficient μ is calculated as the ratio of the measured lateral (tangential) force F_h over the normally applied load F_n. The normal scratch hardness H_n, which is calculated as the ratio of the applied normal force F_n over the vertically projected contact area S_n, i.e., the mean contact pressure in the normal direction, is associated with the resistance to abrasion and plastic deformation during scratching; the lateral scratch hardness H_h, which is calculated as the ratio of the measured tangential force F_h over the horizontally projected contact area S_h, represents the resistance of the material to mechanical deformation in the horizontal direction during scratching. Thus, H_n and H_h are given by Eq. (1) [54]:

$$H_n = F_n/S_n \text{ and } H_h = F_h/S_h \tag{1}$$

Here, S_n and S_h can be calculated from the normal penetration depth d_p as Eq. (2) [55, 56]:

$$S_n = \begin{cases} \pi[R^2 - (R-d_p)^2]/2, & d_p \leqslant d_t \\ \pi(\tan\theta(d_p - d_t) + R/2)^2/2, & d_p > d_t \end{cases}$$
$$S_h = \begin{cases} R^2\arccos((R-d_p)/R) - (R-d_p)\sqrt{R^2-(R-d_p)^2}, & d_p \leqslant d_t \\ \tan\theta((\arcsin\theta - 1)R + d_p)^2 + \pi R^2/6 - R^2/\tan\theta, & d_p > d_t \end{cases} \tag{2}$$

with θ = 60° and R = 108 μm in this work.

Three repeated tests were carried out for each coating with a difference of less than 5% in results because of the excellent quality and uniformity of the prepared coatings. The average values of the results obtained from these three repeated experiments were used in the following analysis.

2.3 DSO algorithm for determining "quantitative" relations

DSO is a symbolic regression analysis framework that uses a deep learning approach and aims to map input variables X ($X_i \in \mathrm{R}^n$) to output variable y ($y_i \in \mathrm{R}$) with a mathematical function f: $\mathrm{R}^n \to \mathrm{R}$ [57]. This approach allows the establishment of "quantitative" relationships among physical variables with experimental data to obtain some insights into the underlying physical mechanisms. In contrast to traditional neural networks, the mapping mechanism relies on the deep symbolic learning (DSR) method. This approach generates symbolic expressions in the form of strings through an iterative optimization process. It employs a recurrent neural network (RNN) from input variables and a set of tokens, which are mathematical operators (e.g., +, −, ×, and ÷), as shown in Fig. 2(a) for an example. With these tokens, a preorder traversal of the binary tree can be constructed, and a "mathematical" formulation describing the relationship between the input and output variables can be established. Additionally, new tokens used as the input for the next RNN can be generated, as schematically illustrated in Fig. 2(b). This completed binary tree, referred to as the sampled expression, is evaluated with the normalized root-mean-square error (NRMSE) as the optimization criterion to determine its applicability, given as Eq. (3):

$$\mathrm{NRMSE} = \frac{1}{\sigma}\sqrt{\frac{1}{n}\sum_{i=1}^{n}(y_i - f(X_i))^2} \tag{3}$$

where σ is the standard deviation of the target value; n is the number of data points; X_i is the i-th input; and y_i is the

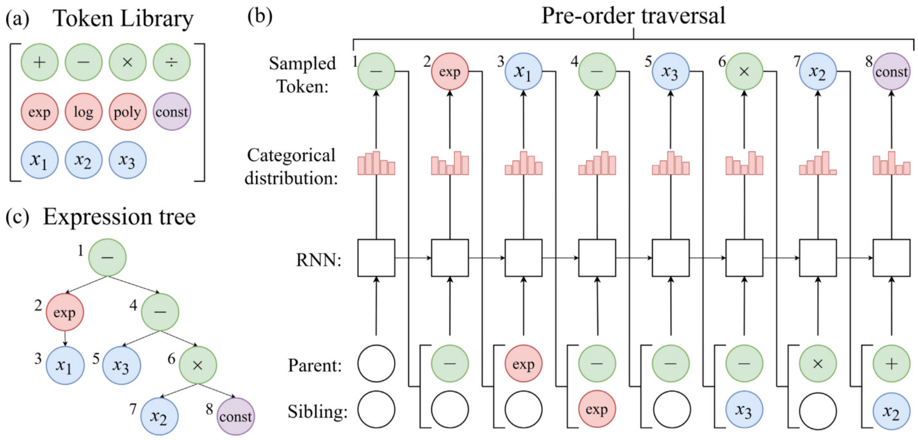

Fig. 2 An example of DSO operation in generating an expression tree: (a) a set of mathematical operation tokens and input variable tokens; (b) generation of a preorder traversal (an initial token is generated by RNN and then used as parent/sibling to generate consecutive tokens until completion of expression tree); (c) expression tree generated by preorder traversal in (b).

corresponding output. The NRMSE is then expressed as a reward function as Eq. (4):

$$R(\tau) = 1/(1 + \text{NRMSE}) \tag{4}$$

where τ represents the sample expression.

The weights and biases of the RNN are adjusted according to the reward function to generate a solution from a higher reward function with a risk-seeking policy gradient algorithm as Eq. (5):

$$\nabla_{\gamma} J_{\text{risk}}(\gamma;\varepsilon) = \mathrm{E}_{\tau\sim p(\tau|\gamma)}\left[(R(\tau) - R_{\varepsilon}(\gamma)) \cdot \nabla_{\gamma} \log p(\tau|\gamma) \,|\, R(\tau) \geqslant R_{\varepsilon}(\gamma)\right] \tag{5}$$

where ∇ represents the gradient operator; γ represents the parameter of the RNN; $J(\gamma;\varepsilon)$ is the learning objective; E[•] represents the expectation value; $R_\varepsilon(\gamma)$ is defined as the $(1-\varepsilon)$-quantile of the distribution of rewards under the current policy; $p(\tau|\gamma)$ is the distribution of mathematical expressions.

3 Results

3.1 Characterization of the coatings by XRD, Raman, and XPS

Figure S2 in the ESM depicts the XRD patterns of the DLCs and MoS_2 coatings. There are three dominant peaks corresponding to the (110), (200), and (220) crystal planes of Fe, which are from the steel substrate. There are no peaks associated with the DLCs in Figs. S2(a) and S2(b) in the ESM, confirming the amorphous state of the DLCs. The XRD patterns shown in Fig. S2(c) in the ESM reveal the crystalline nature of the MoS_2 coating without dopant and with Ti dopant. The XRD peak centered at 12.2° corresponds to the (002) basal plane of MoS_2 [58]. Adding Ti to the Ti/MoS_2 coating reduces the peak intensity, resulting in relatively poor crystallinity and a small crystal size [59].

Figure S3 in the ESM depicts the Raman spectra of the DLCs and MoS_2 coatings. Note that the first and last elements of A and B in A/DLC–B and A/MoS_2–B represent the interlayer and dopant, respectively. According to Figs. S3(a)–S3(g) in the ESM, the Raman spectra of the DLCs can be decomposed into two characteristic peaks. The first peak is the D peak centered at 1,300–1,380 cm^{-1}, which is associated with the breathing vibration mode of the C–C sp^2 ring bond. The second peak is the G peak centered at 1,520–1,580 cm^{-1}, which is associated with the stretching vibration mode of the chain or C–C sp^2 aromatic ring bond. The G peak for the DLCs without dopant is centered at 1,555 cm^{-1}, the same as that reported in Ref. [60], and the D peak for the DLC–Si coatings is centered at 1,370 cm^{-1}, comparable to the 1,373 cm^{-1} reported in Ref. [61]. Table 2 lists the wavenumbers of the D and G peaks (i.e., ω_D and ω_G) and the full width at half maximum (FWHM) of the G peak, which are derived by deconvoluting the corresponding peaks with two Gaussian functions.

Figure S3(h) in the ESM reveals the presence of two characteristic peaks, E^1_{2g} and A_{1g}, which represent the bonding state between the Mo and S atoms within the lattice [58] and corresponds to two characteristic normal modes for the MoS_2 coatings without dopant. The E^1_{2g} peak is the result of in-plane vibrations of Mo and S atoms, and the A_{1g} peak is associated with the out-of-plane vibrations of S atoms [62]. Figure S3(i) in the ESM shows the Raman spectra of the MoS_2 coatings with various dopants (Ti, Pb, and PbTi), in which no distinct characteristic peaks can be observed. The "featureless" curves in the Raman spectra of the doped MoS_2 coatings point to the amorphous structure obtained from the XRD patterns in Fig. S2(c) in the ESM.

Figure S4 in the ESM depicts the XPS analysis of DLCs coatings. Figure S4(a) in the ESM shows the XPS survey spectra of the DLCs with the Si interlayer and various dopants. Note that the DLCs with a Cr interlayer have similar results and thus are not shown in this work. Both the C 1s and O 1s peaks centered at ~284.8 and ~532.0 eV, respectively, are observed in the XPS spectra of all the DLCs, in accordance with the results reported in

Table 2 Raman and XPS parameters obtained for DLCs

DLC	Raman spectra				XPS spectra
	ω_D (cm^{-1})	ω_G (cm^{-1})	I_D/I_G	FWHM (cm^{-1}) of G peak	sp^2/sp^3
Cr/DLC	1,380	1,555	3.0	178	0.8
Cr/DLC–Cr	1,381	1,565	4.6	147	1.0
Cr/DLC–H	1,371	1,544	1.1	154	0.4
Si/DLC	1,384	1,555	3.0	179	0.8
Si/DLC–Si	1,370	1,523	2.0	194	0.5
Si/DLC–Cr	1,381	1,558	4.9	138	1.1
Si/DLC–H	1,376	1,550	0.9	150	0.4

Note: sp^2/sp^3 is the intensity ratio of sp^2 over sp^3 from the XPS spectra, and I_D/I_G is the intensity ratio of D and G bands of the Raman spectra.

清華大学出版社 Tsinghua University Press | SciOpen

Ref. [63]. The C 1s core peak can be deconvoluted into four peaks assigned to C–C sp^3 at ~285.2 eV, C=C sp^2 at ~284.3 eV [64], O–C=O at ~288.2 eV, and C–O–C at ~286.2 eV [65], as shown in Fig. S4(b) in the ESM, for the Si/DLC coating. The Cr 2p peak at ~580 eV [64] for the Cr-doped DLC samples can be deconvoluted into two peaks assigned to Cr 2p$_{1/2}$ for Cr_3C_2 at ~576.8 eV and Cr 2p$_{1/2}$ for metallic Cr at ~574.1 eV [65], as shown in Fig. S4(c) in the ESM for the Si/DLC–Cr coatings. The Si 2p peak at ~100 eV [63] for the Si-doped DLCs can be deconvoluted into Si–O bonds at ~102.0 eV in silicon oxide and Si–C bonds at ~100.1 eV in SiC [66], as shown in Fig. S4(d) in the ESM for the Si/DLC–Si coatings.

Table 2 lists the intensity ratio of C=C sp^2 at ~284.3 eV to C–C sp^3 at ~285.2 eV for the DLCs with two different interlayers and different dopants. The Cr dopant can induce the transformation of sp^3 to sp^2, leading to an increase in the intensity ratio of sp^2/sp^3. The corresponding DLCs become more graphite-like [64]. The H dopant reduces the intensity ratio of sp^2/sp^3, implying that H doping can induce the transformation of sp^2 to sp^3. Adding Si can also induce the transformation of sp^2 to sp^3 to a lesser extent.

Figure S5 in the ESM shows the XPS analysis of the high-resolution XPS survey spectra of the MoS_2 coatings with Ti interlayer and different dopants (i.e., Pb, Ti, and PbTi). Figure S5(a) in the ESM shows the presence of O 1s, C 1s, Mo 3d, and S 2p peaks. Pb 2p was revealed for the Pb-doped and PbTi-codoped MoS_2 coatings. Ti 2p can be seen for the Ti-doped and PbTi-codoped MoS_2 coatings. The C 1s peak is ascribed to ambient contamination [67], and the O 1s peak is due to the absorbed oxygen (molecular oxygen) and the formation of metal oxides [68, 69]. The Mo 3d peak can be deconvoluted into four peaks: Mo 3d$_{3/2}$ at 232.1 eV, Mo 3d$_{5/2}$ at 229.0 eV in MoS_2 (Mo^{4+}) [67, 70], Mo 3d$_{3/2}$ at 235.4 eV, and Mo 3d$_{5/2}$ at 231.9 eV in MoO_3 (Mo^{6+}) [69].

The small hump at ~226.1 eV is the S 2s peak assigned to MoS_2 (S^{2-}) [67], as shown in Fig. S5(b) in the ESM for the Ti/MoS_2 coating without dopant. The deconvolution of the doublet S 2p spectrum of the Ti/MoS_2 coating without dopant reveals two peaks at 161.7 and 162.9 eV, corresponding to S 2p$_{3/2}$ and 2p$_{1/2}$ in MoS_2 (S^{2-}), respectively [71], as shown in Fig. S5(c) in the ESM. The deconvolution of the Pb 4f spectrum shows four peaks: Pb 4f$_{5/2}$ at 143.1 for Pb–Mo–S [70], Pb 4f$_{7/2}$ at 137.5 eV for Pb=O, Pb 4f$_{7/2}$ at 138.5 eV for O=Pb=O, and Pb 4f$_{5/2}$ at 142.4 eV for Pb=S [70], as shown in Fig. S5(d) in the ESM for the Ti/MoS_2–Pb coatings. The deconvolution of the Ti 2p spectrum shows four peaks: Ti 2p$_{1/2}$ at 455.3 eV, Ti 2p$_{3/2}$ at 462.0 eV for Ti_2O_3, Ti 2p$_{1/2}$ at 458.4 eV, and Ti 2p$_{3/2}$ at 464.1 eV for TiO_2 [72].

3.2 Micro-scratch responses of the DLCs and MoS_2 coatings

During the scratching of a coating, the indenter applies normal and tangential forces to the coating. The coating is subjected to tensile stress behind the indenter and shear stress below the indenter [13]. The synergetic effects of these stresses lead to the initiation and propagation of cracks and the separation of the coating from the substrate.

Figure 3 shows optical images of typical residual scratch morphologies for the Cr/DLC and Ti/MoS_2 coatings. There are various damage patterns, including V cracks, peel-off cracks, and semicircular cracks, over the scratch track. The variation in the AE signal with the applied normal load F_n in the corresponding figure shows abrupt changes in the signal strength under certain normal loads, likely indicating the initiation and propagation of scratch-induced surface damage [73]. Table 3 lists three critical loads (L_{c1}, L_{c2}, and L_{c3}) determined from both the optical images of the residual scratch morphologies and the AE signals.

The critical load L_{c1} corresponds to the minimum load for the initiation of periodic V-cracks, at which the AE generally starts to increase and then fluctuates. For $F_n < L_{c1}$, it is difficult to observe surface cracks via optical microscopy, and the AE remains at a constantly low level with negligible fluctuation. The critical load L_{c2} corresponds to the minimum load for the presence of periodic semicircle cracks for the Cr/DLC and Cr/DLC–Cr coatings and peel-off for the other coatings, at which time the AE generally increases abruptly. For $L_{c1} < F_n < L_{c2}$, periodic V-cracks occur on the sides of the groove, and the AE tends to increase with increasing F_n. The critical load L_{c3} represents the bonding strength between the coating and the substrate and can be determined as the minimum load at which partial and periodic (P&P) delamination occurs. The correlation between AE and L_{c3} is complex, and AE normally reaches a high level for the DLCs, whereas it reaches a low level for the MoS_2 coatings.

For $L_{c2} < F_n < L_{c3}$, the periodic V cracks propagate to form semicircular cracks in the center of the groove due to tensile stress behind the indenter for the Cr/DLC and Cr/DLC–Cr coatings; see Fig. 3(a) and Fig. S6(a) in the ESM. Peel-off damage occurs near the edges of the groove for the Cr/DLC–H coating, Si/DLC, and Ti/MoS_2 coatings with different dopants (Fig. 3(b) and Figs. S6(b)–S6(i) in the ESM). The AE reaches a high level with significant fluctuations with increasing F_n due to severe surface cracking for the DLCs, whereas the AE tends to decrease for the Ti/MoS_2 coatings. For $F_n > L_{c3}$, P&P delamination of the coating from the substrate in the center of the groove occurs with the exposure of the substrate, which can be detected as a bright zone

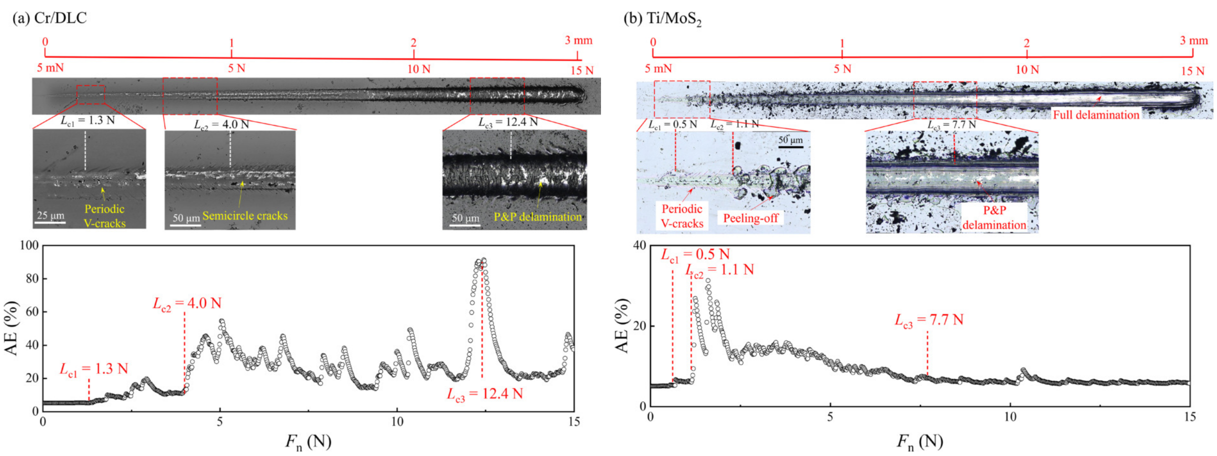

Fig. 3 Optical images of residual scratch morphologies and AE signals of (a) Cr/DLC and (b) Ti/MoS_2 coatings. "P&P" represents "partial and periodic".

due to the severe delamination of the coating in front of the indenter. Only P&P delamination without complete exposure of the substrate under the indenter is observed, and the AE tends to decrease for the Cr/DLCs. Full delamination with complete exposure of the substrate is observed for both the Si/DLCs and Ti/MoS_2 coatings. The AE normally approaches a constantly high level for Si/DLCs because of the continuous and steady delamination of the DLCs, whereas it generally remains at a constantly low level with relatively large fluctuations for the Ti/MoS_2 coatings. Compared with the Si interlayer, the Cr interlayer can better enhance the bonding strength between the coating and the steel substrate since the Cr/DLCs have a larger L_{c3} than the Si/DLCs do. This can be attributed to the Cr interlayer promoting the formation of hard carbide components, which likely increase the bonding strength. Si can react with C and sp^2-C to form sp^3-C–Si, which can enhance the thermal stability of DLCs [74]. Compared with the Si interlayer, the Cr interlayer increases the resistance to delamination in DLCs. Adding H into DLCs impairs the resistance of the DLCs to scratching failure, resulting in weak bonding between the DLCs and the steel substrate, which is consistent with the findings reported in Ref. [13]. Adding Ti and Pd into the Ti/MoS_2 coatings increases L_{c3} and improves the bonding between the MoS_2 coating and the steel substrate.

Figures 4(a)–4(c) show the variation in μ with F_n for the Cr/DLCs, Si/DLCs, and Ti/MoS_2 coatings, respectively. μ increases nonlinearly for $F_n < L_{c2}$, exhibits a linearly increasing trend for $F_n > L_{c2}$, and then remains a linearly increasing trend as F_n increases to the maximum normal load (i.e., 15 N) for the Cr/DLCs, as shown in Fig. 4(a). For the Si/DLCs and Ti/MoS_2 coatings, the linearly increasing trend of μ only holds for $L_{c1} < F_n < L_{c2}$, and μ increases nonlinearly with F_n for $F_n > L_{c3}$, as shown in Figs. 4(b) and 4(c). The full delamination of the coating under large loads led to a nonlinear increase in μ. The partial delamination of the coating was associated with a linear increase in μ for Cr/DLCs.

The average values (μ_M) of the friction coefficient μ for $F_n < L_{c1}$ are also listed in Table 3. A higher μ_M indicates a greater frictional force and more coordinated interaction between the coating and the indenter, making the coating less likely to be delaminated during scratching. Adding Cr, Si, and H into the DLCs can reduce μ_M, and adding Ti, Pb, and PbTi into the MoS_2 coatings has a negligible effect on μ_M for the scratch tests conducted in the ambient environment. These results are different from the findings reported in a previous study in vacuum [58].

Figures 5(a)–5(e) show the variations in F_h, d_r, d_p, H_n, and H_h with the normal load F_n, respectively. Only the results of three representative coatings are presented for clarity since all the coatings exhibit similar trends. The variations in F_h and d_r with F_n can be fitted by piecewise linear functions, as shown in Figs. 5(a) and 5(b), with the intersections as the critical loads L_h and L_r, respectively, whose numerical values are listed in Table 3. The

Table 3 Critical loads for the initiation of various damage modes of DLC and MoS_2 coatings by the Rockwell C 120° indenter under progressive normal loading

Coating	Critical load (N)					k (μm/N)	μ_M	System hardness	
	L_{c1}	L_{c2}	L_{c3}	L_h	L_r			H_{nm} (GPa)	H_{hm} (GPa)
Cr/DLC	1.3	4.0	12.4	8.9	11.4	1.43	0.17	2.2	3.2
Cr/DLC–Cr	1.2	3.1	13.5	10.6	12.2	1.46	0.11	2.2	2.6
Cr/DLC–H	1.1	2.9	8.8	7.1	11.9	1.59	0.11	2.0	1.9
Si/DLC	0.6	2.0	7.1	7.1	11.0	1.52	0.08	2.1	3.5
Si/DLC–Si	1.5	2.2	8.0	9.2	9.6	1.45	0.06	2.2	4.0
Si/DLC–Cr	0.6	3.8	11.2	9.1	9.9	1.49	0.04	2.1	3.4
Si/DLC–H	1.1	3.3	8.0	5.7	9.2	1.41	0.06	2.3	2.6
Ti/MoS_2	0.5	1.1	7.7	6.8	9.7	1.49	0.07	2.2	4.1
Ti/MoS_2–Ti	0.4	1.3	10.4	9.1	11.4	1.57	0.08	2.1	3.7
Ti/MoS_2–Pd	0.3	2.0	8.6	7.3	10.4	1.47	0.08	2.1	3.7
Ti/MoS_2–PdTi	0.7	1.5	10.0	8.4	11.3	1.54	0.08	2.1	3.7

Note: L_{c1} can be determined as the minimum load for the initiation of periodic V-cracks; L_{c2} can be determined as the minimum load for the presence of periodic semicircle cracks for the Cr/DLC and Cr/DLC–Cr coatings and peel-off for other coatings; L_{c3}, associated with the bonding strength between the coating and the substrate, can be determined as the minimum load at which P&P delamination occurs. L_h and L_r are the intersections of the piecewise linear functions for F_h and residual depth d_r vs. F_n, respectively; k is a proportional constant of d_p vs. F_n; μ_M is the mean friction coefficient for $F_n < L_{c1}$; H_{nm} and H_{hm} are the mean values of H_n and H_h for $F_n > L_{c3}$, respectively.

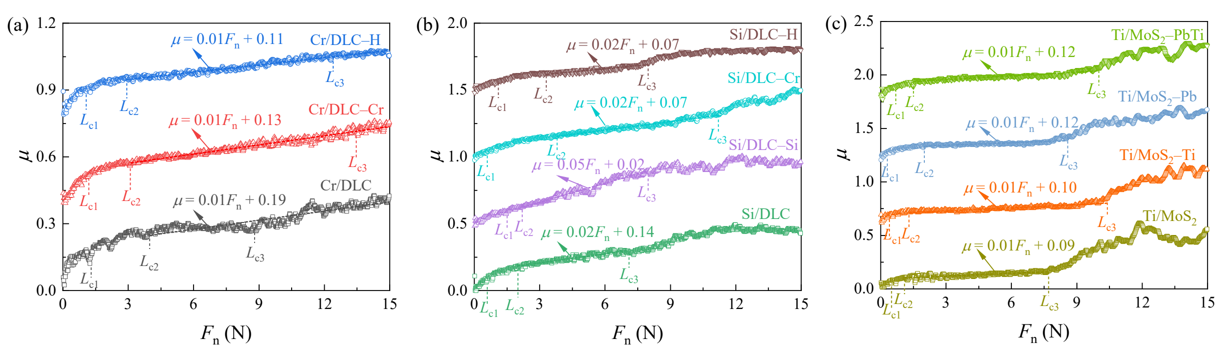

Fig. 4 Variation in μ (the results are shifted for clear display) with normal load F_n for (a) Cr/DLCs (μ is shifted by 0.4, and linear fitting is applied for $F_n > L_{c2}$), (b) Si/DLCs (μ is shifted by 0.5, and linear fitting is applied for $L_{c2} < F_n < L_{c3}$), and (c) Ti/MoS_2 coatings (μ is shifted by 0.6, and linear fitting is applied for $L_{c2} < F_n < L_{c3}$).

value of d_p increases linearly with increasing F_n, as shown in Fig. 5(c), and the numerical values of the proportionality k are listed in Table 3. The penetration depth d_p at $F_n = L_{c1}$ is generally greater than the coating thickness. When $F_n > L_{c3}$, H_n and H_h are significantly affected by the substrate. Both the H_n and H_h of the DLC and MoS_2 coatings approach plateaus under large normal loads. The mean values of H_n and H_h (i.e., H_{nm} and H_{hm}, respectively) for $F_n > L_{c3}$, which can be used to denote the nominal hardness of the coating/substrate system, are also listed in Table 3.

Doping has little effect on H_{nm} under large loads due to delamination of the coating and the exposure of the substrate, which is mainly determined by the penetration resistance of the substrate steel. Since both the DLCs and Ti/MoS_2 coatings have the same steel substrates, the numerical values of H_{nm} are more or less the same for all the coatings studied in this work. Nevertheless, doping has a significant effect on H_{hm}, which is influenced by both the coating and the substrate. The dopants (i.e., Cr and H) can reduce the H_{hm} of the Cr/DLCs, which can be mainly ascribed to the adverse impact of Cr or H on the hardness of the DLCs and is validated by the decrease in H_{hm} due to the presence of Cr or H, as shown in Table 3. The Si/DLC-Si coatings have the largest H_{hm}, indicating that Si has a positive effect on the hardness increase of the DLCs. The Ti/MoS_2 coatings with dopants (i.e., Ti, Pb, and PbTi) have almost the same H_{hm} value, which is smaller than that of the Ti/MoS_2 coatings without any dopant, indicating a negative effect of dopants on the hardness of the Ti/MoS_2 coatings. The DLCs have a larger H_{hm} than the MoS_2 coatings do, which can be explained by the larger d_p of the MoS_2 coatings than the DLCs with a large F_n, as shown in Fig. 5(c).

4 Discussion

Using the data in Tables 1 and 2, we present the linear correlation between the intensity ratio of sp^2/sp^3 determined from the XPS analysis and the I_D/I_G ratio determined from the Raman analysis in Fig. 6. This trend can be explained by the decrease in the number of sp^3 hybrids in DLCs, which can lead to increases in both the intensity ratios of sp^2/sp^3 and I_D/I_G [66]. Notably, sp^3-bonded atoms guarantee increased mechanical strength, and sp^2-bonded atoms ensure good conductivity [75]. A lower intensity ratio of I_D/I_G indicates more sp^3 [76, 77] and thus a small value of the sp^2/sp^3 intensity ratio. Thus, the intensity ratios of I_D/I_G and sp^2/sp^3 of the DLCs are expected to correlate with each other, and smaller values of I_D/I_G and sp^2/sp^3 normally indicate better mechanical properties but lower conductivity and a lower degree of graphene-like characteristics.

Symbolic regression analysis of the scratch results was conducted via the DSO of an open code [57]. The aim was to establish mathematical expressions that best fit the experimental data. The *function_set* was configured to include ["*add*", "*sub*", "*mul*", "*div*", "*const*", "*exp*", "*poly*"]. The optimization process included a polynomial optimizer with a "*poly*" function as a part of the *function_set*. The maximum polynomial degree was set to 3, with a coefficient tolerance of 10^{-6}, and the *dso_least_squares* regressor was used to fit the data. The NRSME threshold for the early stopping parameter was set to 10^{-16}. The reward function was set as the inverse normalized root mean square error (*inv_nrmse*), which can optimize the expressions by minimizing the error between the predicted and actual values. The metric parameters were set to [1.0]. Training hyperparameters is crucial for effective model learning. A significantly large sample size of 8×10^6 was used, with a batch size of 1,000 and an epsilon parameter of 0.05, to balance exploration and exploitation. The policy optimizer's learning rate was 5×10^{-4} with an entropy weight of 0.03 and an entropy decay factor (*entropy_gamma*) of 0.7.

The scratch response of a coating is known to be dependent on the coating thickness and material parameters. Using DSO analysis with DSR deep learning, the scratch responses of the coating, as listed in Table 3, were correlated with the parameters given in Tables 1 and 2. The DSO analysis revealed that L_{c1}, k, and μ_M of the DLCs are functions of three material parameters of the FWHM of the G peak, and the intensity ratios of I_D/I_G and sp^2/sp^3 can be empirically expressed as Eqs. (6)–(9):

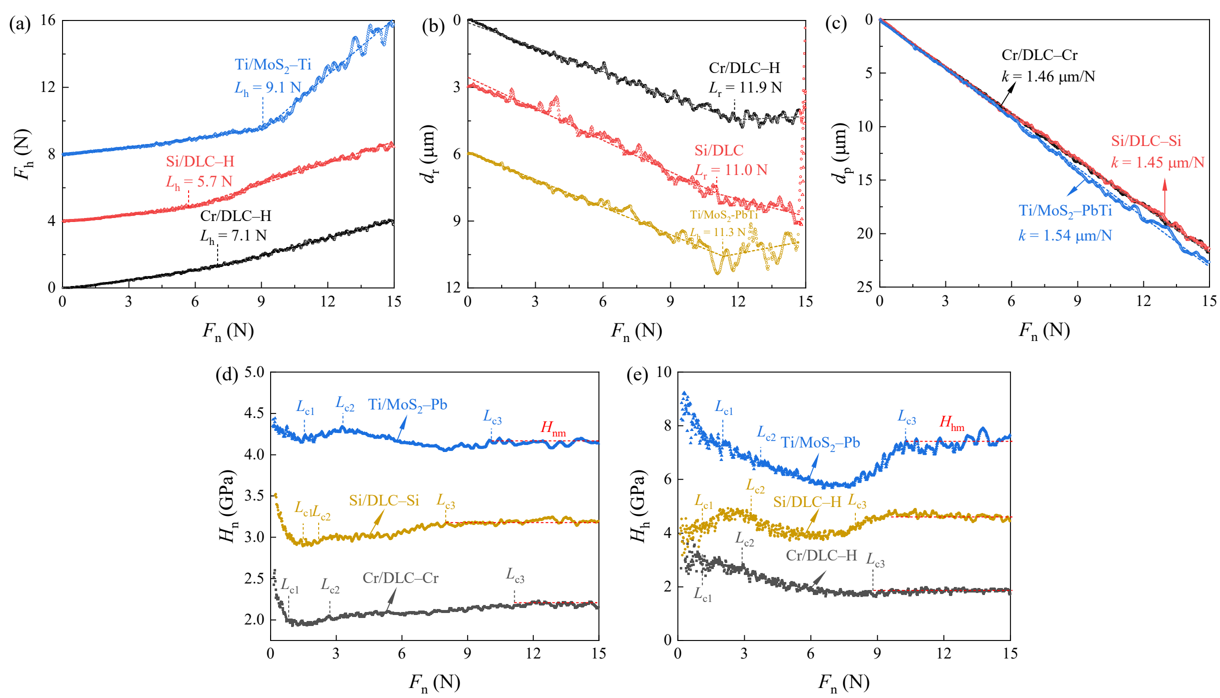

Fig. 5 Variations in scratch variables with normal load F_n (only results of three different coatings are presented for clarity): (a) F_h (F_h is shifted by 4 N), (b) d_r (d_r is shifted by 3 μm), (c) d_p, (d) H_n (H_n is shifted by 1 GPa), and (e) H_h (H_h is shifted by 2 GPa).

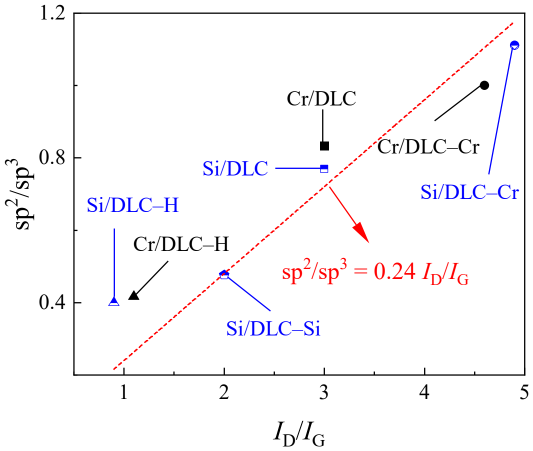

Fig. 6 Correlations between I_D/I_G and sp^2/sp^3.

$$L_{c1} = -s + (I-1.63)\left(-ws^3 + 332.72s^4 - 847.22s^3 + 875.56s^2 - 213.66s\right) + 1 \quad (6)$$

$$k = I^2 + \frac{Iw}{4.44 - I^4 s\left(0.1001I^4 - 0.7321I^3 + 1.0981I^2 - 0.7786\right)^{-1}} - 25.49 \quad (7)$$

$$\mu_M = (4.4782 - I)\left[P(s-0.4188) + 0.1678\right] \quad (8)$$

$$P = ws(0.6383s - 0.0611Is - 0.5565) - 0.0057w + 28.2895 \quad (9)$$

where k (μm/N) is the proportional coefficient of d_p vs. F_n; w is the FWHM (cm^{-1}) of the G peak; I is the intensity ratio of I_D/I_G; s is the intensity ratio of sp^2/sp^3. These results can be attributed to the negligible effect of the substrate on L_{c1} and μ_M under relatively low loads, which can be regarded as the "intrinsic" characteristics of the DLCs. The steel substrate has few effects on the linear relationship between d_p and F_n for hard and brittle DLCs. The correlations of Eqs. (6)–(8) allow for the determination of the FWHM of the G peak, I_D/I_G, and sp^2/sp^3 if the numerical values of L_{c1}, k, and μ_M can be determined from scratch tests. Note that Eqs. (6)–(8) are only applicable to DLCs.

Notably, Raman shift has been used to characterize the mechanical behavior of materials. For example, Du et al. [78] analyzed the mechanical behavior of a graphene/MoS_2 heterostructure from the perspective of the dependence of Raman and photoluminescence spectra on the strain state. Yang et al. [79] discussed the strain effect on the Raman shift of graphene. Ferralis [80] revealed that the Grüneisen parameter and shear deformation potential of graphene films can be determined through the Raman peak shift, and the lattice strain in the graphene films can be directly measured through the change in Raman peaks. Bi et al. [81] applied Raman spectroscopy to assess the fracture resistance of bones. Fang et al. [82] applied the mechano-Raman spectroscopy technique to correlate micromechanical properties with Raman parameters. However, few studies have correlated the results of Raman spectroscopy and XPS with scratch responses.

For $F_n > L_{c3}$, the DSO analysis yields (Eq. (10)):

$$H_{hm} = \mu_M\left(-t + \exp\left(54.8k\mu_M^2 t^3 - 147\mu_M^2 t^3 + 4.50\mu_M t^3 - 0.30t^3 + 3.09t\right) + 22.2\right) - 0.22 \quad (10)$$

which is an empirical correlation between H_{hm} and a group of material parameters. The mean lateral scratch hardness, H_{hm} (GPa), is dependent on three main parameters: μ_M, coating thickness t (μm), and k (μm/N). This can be attributed to the fact that the coating thickness, contact friction, and plastic deformation play key roles in lateral deformation under large loads or penetration depths.

Figure S7 in the ESM depicts the variation in H_{hm} with the coating thickness t for 1 μm ⩽ t ⩽ 3 μm for the Ti/MoS_2–Pb coating when k = 1.47 μm/N and μ_M = 0.08, as shown in Table 3. When t is less than 1.6 μm, H_{hm} increases with increasing t, likely indicating a surface effect. For t larger than 1.6 μm, H_{hm} decreases with increasing t, which can be explained by the fact that a thicker coating can likely have more defects/flaws due to internal stress and limited bonding strength at the interface [83] and is more vulnerable to delamination under high loads. As delamination occurs, the contribution of the coating to the overall hardness diminishes, indicating that an increase in t leads to a decrease in H_{hm}.

According to the DSO analysis, the critical load L_{c3} as a function of L_h, t, and L_r can be expressed as Eq. (11):

$$L_{c3} = -L_h + 1.26t(L_h - 7.08) - \frac{4{,}350(9.5 - L_r)}{L_h + 264L_r - 2{,}508} \quad (11)$$

Equation (11) provides an empirically simple way to determine the critical load of L_{c3} from the experimental data instead of estimation with the help of photographs. With a known coating thickness, L_{c3} can be determined in a more accurate way from analyzing scratch data rather than from detection with the aid of a microscope. Notably, the coating thickness might play a role in the measurement of the adhesion strength L_{c3} [84], highlighting the importance of the coating thickness when comparing the adhesion strength between different coatings and the substrates. Both L_h and L_r are dependent on the coating thickness, highlighting the importance of specifying the coating thickness when comparing the bonding strengths of different coatings.

Equations (10) and (11) are for both the DLCs and MoS_2 coatings of approximately 2 μm in thickness, even though the DLCs exhibit different mechanical behaviors from the MoS_2 coatings. Additionally, the mathematical formulations obtained from DSO analysis and other machine learning methods are limited by the scope of the data available. It is often difficult to justify the applicability of formulations out of the data range. Equations (10) and (11) are suggested to be applicable to coatings with thicknesses in the range of 1–3 μm, according to the coating thicknesses studied in this work (Table 1). Thus, the applicability of the equations for coatings with thicknesses outside of the currently studied range (e.g., submicrometer or more than 5 μm thick coatings) requires further studies, which may need to include the contributions of size-dependent mechanical properties [85] and surface roughness [86]. Nevertheless, the explicit formula obtained from the DSO analysis in this work has many advantages over traditional "black box" neutral network models for application and verification in future work.

Figure S8 in the ESM presents comparisons of the data obtained from the mathematical formulations and the experimental data from the micro-scratch tests for L_{c3}, H_{hm}, L_{c1}, k, and μ_M, which show excellent agreement between the calculated results and the measurement results. Moreover, the coating thickness can be derived from the experimental results of H_{hm}, k, and μ_M or L_{c3}, L_h, and L_r, which paves the way for using a scratch-based approach to determine the coating thickness. However, multiscale and multiphysics modeling approaches [87–89] are still needed to investigate the physical mechanisms involved in elucidating the relationships between the microstructures and mechanical responses of coatings, even though DSO analysis can provide nominal "mathematical" formulations describing the complex and synergetic effects of coating thickness and material parameters on the scratch responses of coatings.

5 Conclusions

In summary, we characterized the effects of dopants and interlayers on the microstructures and scratch behavior of DLCs and Ti/MoS_2 coatings on 304 stainless steels. The DLCs doped with Si, Cr, or H remain amorphous, whereas the addition of Ti, Pb, or PbTi to the MoS_2 coatings leads to the formation of an amorphous structure. The analysis of the XPS survey and Raman spectra revealed that the intensity ratio of sp^2/sp^3 by XPS is proportional to the intensity ratio of I_D/I_G by the Raman spectra of the DLCs. Doping Cr in DLCs can induce the transformation of sp^3 to sp^2, and doping H or Si can induce the transformation of sp^2 to sp^3.

Three critical loads describing the scratch-induced damage, corresponding, respectively, to the initiation of periodic V-cracking, the minimum load for periodic semicircle cracking or peel-off, and the minimum load for partial and periodic delamination, have been determined from the optical images of the residual scratch tracks and AE signals. The friction coefficient μ is strongly correlated with the critical load: μ increases nonlinearly for $F_n < L_{c2}$, linearly increases for $F_n > L_{c2}$, and then linearly increases as F_n increases to the maximum applied load for the Cr/DLCs. For the Si/DLCs and Ti/MoS_2 coatings, the linear increasing trend only holds for $L_{c1} < F_n < L_{c2}$, and μ increases nonlinearly with F_n for $F_n > L_{c3}$. Dopants can reduce the friction coefficient of DLCs and have a negligible effect on Ti/MoS_2 coatings. The bonding strength between the DLCs and the steel substrates can be better enhanced by the Cr interlayer than by the Si interlayer. Doping Cr and H can reduce the hardness of DLCs; doping Si can increase the hardness of DLCs; and doping Ti, Pb, and PbTi can reduce the hardness of MoS_2 coatings.

The DSO analysis of the scratch results led to the establishment of nominal "mathematical" formulations between the critical variables H_{hm}, L_{c3}, L_{c1}, k, and μ_M and the material parameters t, I_D/I_G, the FWHM of the G peak, and sp^2/sp^3. The critical variables L_{c1}, k, and μ_M of the DLCs are independent of the coating thickness t. These relationships allow for the determination of the FWHM of the G peak, I_D/I_G, and sp^2/sp^3 as well as the coating thickness if the numerical values of the critical variables can be determined from scratch tests. The results obtained in this work can aid further investigation and optimization of DLCs and Ti/MoS_2 coatings with tailored properties for advanced engineering applications via scratch-based methodology. DSO analysis provides a "deep learning" way to establish "quantitative" relationships between the critical variables of scratch tests and the scratch parameters as well as material parameters.

CRediT authorship contribution statement

Ming Liu: conceptualization, data curation, formal analysis, funding acquisition, investigation, methodology, resources, supervision, validation, and writing - review & editing. Zhitong Xu: data curation, formal analysis, investigation, visualization, and writing - original draft. Noraphat Yuktanan: formal analysis, visualization, and writing - original draft. Tang Gu: formal analysis, funding acquisition, methodology, resources, supervision, and writing - review & editing. Guangan Zhang: funding acquisition, resources, and supervision. Jinyang Jiang: resources, validation, and supervision. Fuqian Yang: formal analysis, supervision, validation, and writing - review & editing. Rui Liang: funding acquisition, project administration, resources, supervision, and writing - review & editing.

Data availability

The data that support the findings of this study are available from the corresponding author upon reasonable request.

Declaration of competing interest

The authors have no competing interests to declare that are relevant to the content of this article.

Acknowledgements

Rui Liang is grateful for the support from the Science and Technology Development Fund, Macao SAR (File No. 0019/2023/AMJ). Ming Liu is grateful for support from the National Natural Science Foundation of China (No. 51705082). Tang Gu is grateful for the support of the National Natural Science Foundation of China (No. 12302093). Guangan Zhang is grateful for the National Natural Science Foundation of China (No. 52275221).

Electronic Supplementary Material

Supplementary material (the determination of the coating thickness, XRD spectra, XPS survey spectra, Raman spectra, and optical micrographs with AE signals of DLC and MoS_2 coatings; variation in H_{hm} with the coating thickness t in the range of 1 μm ≤ t ≤ 3 μm for the Ti/MoS_2–Pb coatings, using k = 1.47 μm/N and μ_M = 0.08 from Table 3; comparisons of the data obtained from the mathematical formulations and the experimental data from the microscratch tests for L_{c3}, H_{hm}, L_{c1}, k, and μ_M, respectively) is available in the online version of this article at https://doi.org/10.26599/FRICT.2025.9441166.

References

[1] Zhang M L, Wei X B, Kong L G, Zhang G G, Wang Y, Wu Z G. Improvement on uniformity of diamond-like carbon coatings inside metal tubes using high power pulse supply. *Appl Phys A* **126**(8): 597 (2020)

[2] Zhang J G, Han G F, Cao X X, Zhang X F, Zhang J D, Liu M, Zhou K S. Regulating the composition, structure, and nanoscale dimensions of $Yb_2Si_2O_7$ environmental barrier coating to achieve a biomimetic teakwood-like functional structure by waste gas recycling. *J Adv Ceram* **14**(2): 9221021 (2025)

[3] Ye Z Y, Wang S Q, Yu S, Zhao X R, Zou Y C, Chen G L, Wen L, Zhao L N, Zhang G X, Wang Y M, et al. HfC–HfO_2 modified high/superhigh temperature thermal protection coating for superior hot corrosion resistance and antioxidation performance. *J Adv Ceram* **14**(1): 9221014 (2025)

[4] Thukral T S, Rabbi K F, Khodakarami S, Yang W T, Sudarshan A, Pitschman M A, Fourspring P M, Miljkovic N. Scalable and durable polydimethylsiloxane coating for anti-corrosion, anti-fouling, and condensation applications. *Cell Rep Phys Sci* **5**(10): 102243 (2024)

[5] Dong L, Yang W Q, Chen L, Yang G J, Li C J. Realizing the excellent oxidation resistance of an environmental barrier coating through aluminum surface modification. *J Adv Ceram* **13**(7): 976–986 (2024)

[6] Li R J, Hu C W, Gao L Y, Zhang Y L, Zhang P, Fan Z J, Liu J, Zhao X D, Ma S H, Zhou F. *In situ* manufacture of hydrogel lubrication coating on damaged tissue to resist adhesion. *Cell Rep Phys Sci* **5**(7): 102040 (2024)

[7] Li W H, Lin C J, Ma W, Li Y, Chu F Q, Huang B L, Yao S H. Transparent selective photothermal coatings for antifogging applications. *Cell Rep Phys Sci* **2**(5): 100435 (2021)

[8] Dong X C, Zhao Q H, Li Y, Gu S M, Xu X M, He D W, Ye F, Cheng L

F, Luan X G, Yu Z J. Fabrication and high temperature electrical conductivity of polymer-derived SiHfBCN ceramic coating. *J Adv Ceram* **14**(1): 9221011 (2025)

[9] Dong K C, Tseng D, Li J C, Warkander S, Yao J, Wu J Q. Reducing temperature swing of space objects with temperature-adaptive solar or radiative coating. *Cell Rep Phys Sci* **3**(10): 101066 (2022)

[10] Bernal R A, Chen P L, Schall J D, Harrison J A, Jeng Y R, Carpick R W. Influence of chemical bonding on the variability of diamond-like carbon nanoscale adhesion. *Carbon* **128**: 267–276 (2018)

[11] Zhuang W H, Li H, Li W, Fan X Q, He J F, Cai Z B, Fu W, Zhang G G, Wan S H, Zhu M H. Probing fretting performance of DLC and MoS_2 films under fluid lubrication. *Appl Surf Sci* **478**: 661–679 (2019)

[12] Jiang A H, Cao X L, Wang Z Y, Ma J F, Xiao J R, Ma S S. Friction performance and corrosion resistance of MoS_2/DLC composite films deposited by magnetron sputtering. *Results Phys* **25**: 104278 (2021)

[13] Liu M, Xu Z T, Zhang G G. Effects of dopants on scratch responses of diamond-like carbon films by Rockwell C diamond indenter. *J Mater Eng Perform* **32**(13): 6092–6106 (2023)

[14] Su Y Y, Gong X H, Huang W J, Zhang T F, Hu R, Zhang P, Ruan H B, Ma Y C. Enhancing the tribological property of Mo-doped DLC films in methanol using appropriate bias voltage. *Diam Relat Mater* **135**: 109795 (2023)

[15] Kim J I, Lee W Y, Tokoroyama T, Umehara N. Long-term low-friction of Ti-overcoated and-doped DLCs: Robustly developed carbonous transfer layer with titanium. *Carbon* **204**: 2268–283 (2023)

[16] Yetim A F, Kovacı H, Kasapoğlu A E, Bozkurt Y B, Çelik A. Influences of Ti, Al and V metal doping on the structural, mechanical and tribological properties of DLC films. *Diam Relat Mater* **120**: 108639 (2021)

[17] Gao Y, Liu S S, Liao J H, Zhao D Y, Liu J G. High temperature tribological properties of modified CF in MoS_2 composite coating. *Tribology* **44**(4): 482–493 (2024) (in Chinese)

[18] Su Y L, Kao W H. Tribological behaviour and wear mechanism of MoS_2–Cr coatings sliding against various counterbody. *Tribol Int* **36**(1): 11–23 (2003)

[19] Maas P, Mizumoto Y, Kakinuma Y, Min S. Anisotropic brittle-ductile transition of monocrystalline sapphire during orthogonal cutting and nanoindentation experiments. *Nanotechnol Precis Eng* **1**(3): 157–171 (2018)

[20] Xue L L. Study of the material removal mechanism of glass-ceramics based on consecutive incremental loading in ductile-regime grinding. *Nanotechnol Precis Eng* **3**(2): 88–95 (2020)

[21] Liu M, Yan F W. Scratch-induced deformation and damage behavior of doped diamond-like carbon films under progressive normal load of Vickers indenter. *Thin Solid Films* **756**: 139351 (2022)

[22] Segura-Giraldo B, Restrepo-Parra E, Arango-Arango P J. On the influence of a TiN interlayer on DLC coatings produced by pulsed vacuum arc discharge: Compositional and morphological study. *Appl Surf Sci* **256**(1): 136–141 (2009)

[23] Wang X Y, Sui X D, Zhang S T, Yan M M, Lu Y, Hao J Y, Liu W M. Impacts of the a-Si: H interlayer nanostructure on the adhesion of the thick DLC coatings prepared by PECVD. *Appl Surf Sci* **565**: 150539 (2021)

[24] Chang S Y, Yan Y D, Geng Y Q. Cutting, nanoexfoliation, and reshaping of multilayer MoS_2 using atomic force microscopy-based thermomechanical scratch. *ACS Appl Nano Mater* **7**(23): 27142–27153 (2024)

[25] Kim S H, Ahn H S. Nanotribological properties and scratch resistance of MoS_2 bilayer on a SiO_2/Si substrate. *Friction* **11**(1): 154–164 (2023)

[26] Renevier N M, Fox V C, Teer D G, Hampshire J. Coating characteristics and tribological properties of sputter-deposited MoS_2/metal composite coatings deposited by closed field unbalanced magnetron sputter ion plating. *Surf Coat Tech* **127**(1): 24–37 (2000)

[27] Stoyanov P, Strauss H W, Chromik R R. Scaling effects between micro- and macro-tribology for a Ti–MoS_2 coating. *Wear* **274**: 149–161 (2012)

[28] Rovinelli A, Sangid M D, Proudhon H, Ludwig W. Using machine learning and a data-driven approach to identify the small fatigue crack driving force in polycrystalline materials. *NPJ Comput Mater* **4**: 35 (2018)

[29] Pei X J, Cao Y D, Gu T, Xie M J, Dong P S, Wei Z G, Mei J F, Zhang T R. Generalizing multiaxial vibration fatigue criteria in the frequency domain: A data-driven approach. *Int J Fatigue* **186**: 108390 (2024)

[30] Feng Z W, Gu T, Zhao D, Liu S G. Prediction of the hydrogen affected S–N curve based on MLP-regressor model for type 316 stainless steel. In: Proceedings of the International Conference on Marine Equipment & Technology and Sustainable Development, 2023: 94–104.

[31] Guo C, Liu S G, Zou Y, Zhao D, Cheng M S, Gu T, Liu Y X, Zhang Q Q, Wang Q H, Feng Z W. Fatigue properties and life prediction of GS80A steel under the effect of hydrogen-rich environment. *JOM* **75**(4): 1306–1318 (2023)

[32] Feng Z, Li X F, Song X L, Gu T, Zhang Y. Hydrogen embrittlement of CoCrFeMnNi high-entropy alloy compared with 304 and IN718 alloys. *Metals* **12**(6): 998 (2022)

[33] Li X F, Wang C Y, Feng H, Gu T, Zhang J, Zhang Y, Ren X C. Simultaneously enhancing strength and hydrogen embrittlement resistance of pure iron *via* gradient microstructure. *Corros Sci* **218**: 111134 (2023)

[34] Guo C, Liu S G, Gu T, Zhou L H, Zhao D, Dong L Q, Zhang Q Q, Wang Q H, Ling C. Coupled effects of hydrogen embrittlement and temperature and surface roughness on the mechanical properties of GS80A steel. *Eng Fail Anal* **160**: 108112 (2024)

[35] Qin J H, Zhang J W, Li Y X, Cao X Y, Qiao Z Y. Prediction of scratch responses of metallic material based on machine learning. *Tribology* **43**(12): 1445–1452 (2023) (in Chinese)

[36] Zhang J W, Qin J H, Li Y X, Lu C S, Liu H T, Zhao M H. Extraction of the plastic properties of metallic materials from scratch tests using deep learning. *Mech Mater* **175**: 104502 (2022)

[37] Pan Z F, Yang J, Wang X E, Wang F L, Azim I, Wang C Y. Image-based surface scratch detection on architectural glass panels using deep learning approach. *Constr Build Mater* **282**: 122717 (2021)

[38] Parsazadeh M, Fisher G, McDonald A, Hogan J. Computational investigation of the effect of microstructure on the scratch resistance of tungsten-carbide nickel composite coatings. *Wear* **478**: 203888 (2021)

[39] Kitzelmann E. Inductive programming: A survey of program synthesis techniques. In: *Approaches and Applications of Inductive Programming. Lecture Notes in Computer Science, Vol. 5812*. Schmid U, Kitzelmann E, Plasmeijer R, Eds. Springer Berlin Heidelberg, 2010: 50–73.

[40] Koza J R. Genetic programming as a means for programming computers by natural selection. *Stat Comput* **4**(2): 87–112 (1994)

[41] Mundhenk T N, Landajuela M, Glatt R, Santiago C P, Faissol D M, Petersen B K. Symbolic regression via neural-guided genetic programming population seeding. In: Proceedings of the 35th International Conference on Neural Information Processing Systems, 2021.

[42] Schmidt M, Lipson H. Distilling free-form natural laws from experimental data. *Science* **324**(5923): 81–85 (2009)

[43] Brunton S L, Proctor J L, Kutz J N. Discovering governing equations from data by sparse identification of nonlinear dynamical systems. *P Natl Acad Sci USA* **113**(15): 3932–3937 (2016)

[44] Petersen B K, Landajuela M, Mundhenk T N, Santiago C P, Kim S K, Kim J T. Deep symbolic regression: Recovering mathematical expressions from data via risk-seeking policy gradients. In: Proceedings of the International Conference on Learning Representations, 2019.

[45] Landajuela M, Lee C S, Yang J C, Glatt R, Santiago C, Aravena I, Mundhenk T N, Mulcahy G, Petersen B K. A unified framework for

deep symbolic regression. In: Proceedings of the 36th International Conference on Neural Information Processing Systems, 2022: 33985–33998.
[46] Lu Q, Luo Y Z, Li H Y, Luo J, Wang Z G. Deep differentiable symbolic regression neural network. *Neurocomputing* **629**: 129671 (2025)
[47] Liu H Y, Liu H Y, Kuang Y F, Wang J, Li B. Deep symbolic optimization for combinatorial optimization: Accelerating node selection by discovering potential heuristics. In: Proceedings of the Genetic and Evolutionary Computation Conference Companion, 2024: 2067–2075.
[48] Melching D, Paysan F, Strohmann T, Breitbarth E. An iterative crack tip correction algorithm discovered by physical deep symbolic regression. *Int J Fatigue* **187**: 108432 (2024)
[49] Abdusalamov R, Weise J, Itskov M. Rediscovering the Mullins effect with deep symbolic regression. *Int J Plasticity* **179**: 104037 (2024)
[50] Liu M, Yan F W. Comparison of microscratch responses of metals between berkovich and Rockwell C indenters under progressive normal force. *Tribol Lett* **69**(4): 157 (2021)
[51] Bhattacharyya A S, Bhattacharyya K. Effect of loading rate and coating thickness on wear and adhesion during sliding indents of Si–C–N/glass coatings useful for automotive applications. *Results Surf Interfaces* **14**: 100196 (2024)
[52] Kumar A, Vostrak M, Houdkova S. Evaluating fracture toughness of cold sprayed IN625 coatings: Micro-scratching method. *Eng Mater Des* **247**: 113430 (2024)
[53] Liu M, Zheng Q, Gao C H. Sliding of a diamond sphere on fused silica under ramping load. *Mater Today Commun* **25**: 101684 (2020)
[54] Liu M, Xu Z T. Micromechanical characterization of microwave dielectric ceramic $BaO–Sm_2O_3–5TiO_2$ by indentation and scratch methods. *J Adv Ceram* **12**(6): 1136–1165 (2023)
[55] Liu M. Microscratch of copper by a Rockwell C diamond indenter under a constant load. *Nanotechnol Precis Eng* **4**(3): 033003 (2021)
[56] Liu M, Hou D Y, Wu L X. Influence of poly(ethyleneimine) functionalized multi-walled carbon nanotubes on mechanical and tribological behavior of epoxy resins. *Mater Today Commun* **33**: 104480 (2022)
[57] Petersen B K, Landajuela M, Mundhenk T N, Santiago C P, Kim S K, Kim J T. Deep symbolic regression: Recovering mathematical expressions from data via risk-seeking policy gradients. In: Proceedings of the 9th International Conference on Learning Representations, 2021: 1–26.
[58] Ren S M, Li H, Cui M J, Wang L P, Pu J B. Functional regulation of Pb-Ti/MoS_2 composite coatings for environmentally adaptive solid lubrication. *Appl Surf Sci* **401**: 362–372 (2017)
[59] Zhao X Y, Lu Z B, Zhang G G, Wang L P, Xue Q J. Self-adaptive MoS_2–Pb–Ti film for vacuum and humid air. *Surf Coat Tech* **345**: 152–166 (2018)
[60] Gayathri S, Kumar N, Krishnan R, Ravindran T R, Dash S, Tyagi A K, Sridharan M. Influence of Cr content on the micro-structural and tribological properties of PLD grown nanocomposite DLC–Cr thin films. *Mater Chem Phys* **167**: 194–200 (2015)
[61] Choi J, Nakao S, Miyagawa S, Ikeyama M, Miyagawa Y. The effects of Si incorporation on the thermal and tribological properties of DLC films deposited by PBII&D with bipolar pulses. *Surf Coat Tech* **201**(19–20): 8357–8361 (2007)
[62] Cho K, Min M, Kim T Y, Jeong H, Pak J, Kim J K, Jang J, Yun S J, Lee Y H, Hong W K, et al. Electrical and optical characterization of MoS_2 with sulfur vacancy passivation by treatment with alkanethiol molecules. *ACS Nano* **9**(8): 8044–8053 (2015)
[63] Zhang T F, Wan Z X, Ding J C, Zhang S H, Wang Q M, Kim K H. Microstructure and high-temperature tribological properties of Si-doped hydrogenated diamond-like carbon films. *Appl Surf Sci* **435**: 963–973 (2018)
[64] Zou C W, Wang H J, Feng L, Xue S W. Effects of Cr concentrations on the microstructure, hardness, and temperature-dependent tribological properties of Cr–DLC coatings. *Appl Surf Sci* **286**: 137–141 (2013)
[65] Singh V, Jiang J C, Meletis E I. Cr-diamondlike carbon nanocomposite films: Synthesis, characterization and properties. *Thin Solid Films* **489**(1–2): 150–158 (2005)
[66] Fayed S M, Chen D X, Li S L, Sadawy M M, Eid E A. Microstructure, mechanical, and electrochemical properties of Si/DLC coating deposited on 2024-T3 Al alloy. *J Alloys Compd* **966**: 171452 (2023)
[67] Qin X P, Ke P L, Wang A Y, Kim K H. Microstructure, mechanical and tribological behaviors of MoS_2–Ti composite coatings deposited by a hybrid HIPIMS method. *Surf Coat Tech* **228**: 275–281 (2013)
[68] Li H, Zhang G G, Wang L P. Low humidity–sensitivity of MoS_2/Pb nanocomposite coatings. *Wear* **350**: 1–9 (2016)
[69] Feng X G, Wang R, Wei G, Zheng Y G, Hu H J, Yang L, Zhang K F, Zhou H. Effect of a micro-textured surface with deposited MoS_2–Ti film on long-term wear performance in vacuum. *Surf Coat Tech* **445**: 128722 (2022)
[70] Wang Z, Cai Z B, Sun Y, Peng J F, Zhu M H. Low velocity impact wear behavior of MoS_2/Pb nanocomposite coating under controlled kinetic energy. *Surf Coat Tech* **326**: 53–62 (2017)
[71] Wong K C, Lu X, Cotter J, Eadie D T, Wong P C, Mitchell K A R. Surface and friction characterization of MoS_2 and WS_2 third body thin films under simulated wheel/rail rolling–sliding contact. *Wear* **264**(7–8): 526–534 (2008)
[72] Bertóti I, Mohai M, Sullivan J L, Saied S O. Surface characterisation of plasma-nitrided titanium: An XPS study. *Appl Surf Sci* **84**(4): 357–371 (1995)
[73] Stallard J, Poulat S, Teer D G. The study of the adhesion of a TiN coating on steel and titanium alloy substrates using a multi-mode scratch tester. *Tribol Int* **39**(2): 159–166 (2006)
[74] Dai W, Gao X, Liu J M, Wang Q M. Microstructure, mechanical property and thermal stability of diamond-like carbon coatings with Al, Cr and Si multi-doping. *Diam Relat Mater* **70**: 98–104 (2016)
[75] Bu H X, Zheng H B, Zhou H C, Zhang H Y, Yang Z F, Liu Z E, Wang H, Xu Q. The role of sp^2 and sp^3 hybridized bonds on the structural, mechanical, and electronic properties in a hard BN framework. *RSC Adv* **9**(5): 2657–2665 (2019)
[76] Ferrari A C, Robertson J. Interpretation of Raman spectra of disordered and amorphous carbon. *Phys Rev B* **61**(20): 14095–14107 (2000)
[77] Irmer G, Dorner-Reisel A. Micro-Raman studies on DLC coatings. *Adv Eng Mater* **7**(8): 694–705 (2005)
[78] Du H Z, Kang Y L, Xu C C, Xue T, Qiu W, Xie H M. Measurement and characterization of interfacial mechanical properties of graphene/MoS_2 heterostructure by Raman and photoluminescence (PL) spectroscopy. *Opt Lasers Eng* **149**: 106825 (2022)
[79] Yang K L, Lee J O, Choo H, Yang F Q. Can Raman shift be used to characterize the mechanical property of graphene. *J Phys Chem C* **122**(42): 24467–24474 (2018)
[80] Ferralis N. Probing mechanical properties of graphene with Raman spectroscopy. *J Mater Sci* **45**(19): 5135–5149 (2010)
[81] Bi X H, Patil C A, Lynch C C, Pharr G M, Mahadevan-Jansen A, Nyman J S. Raman and mechanical properties correlate at whole bone- and tissue-levels in a genetic mouse model. *J Biomech* **44**(2): 297–303 (2011)
[82] Fang S S, Duan S, Wang X Z, Chen S J, Li L, Li H, Jiang B C, Liu C H, Wang N Y, Zhang L, et al. Direct characterization of shear phonons in layered materials by mechano-Raman spectroscopy. *Nat Photonics* **17**(6): 531–537 (2023)
[83] Vaz R F, Garfias A, Albaladejo V, Sanchez J, Cano I G. How increasing cold spray coatings thickness affects their residual stress and properties. *Surf Coat Tech* **485**: 130867 (2024)
[84] Demirci I, Gauthier C, Schirrer R. Mechanical analysis of the damage of a thin polymeric coating during scratching: Role of the ratio of the

coating thickness to the roughness of a scratching tip. *Thin Solid Films* **479**(1–2): 207–215 (2005)
[85] Sahoo P, Kumar S, Singh R K, Srinivas G, Bonu V, Barshilia H C. Effect of arc-deposited diamond-like carbon (DLC) coating thickness on friction and size effects in high-speed micromilling of Ti_6Al_4V. *Tribol Int* **192**: 109223 (2024)
[86] Shahsavari F, Ehteshamzadeh M, Naimi-Jamal M R, Irannejad A. Nanoindentation and nanoscratch behaviors of DLC films growth on different thickness of Cr nanolayers. *Diam Relat Mater* **70**: 76–82 (2016)
[87] Gu T, Medy J R, Klosek V, Castelnau O, Forest S, Hervé-Luanco E, Lecouturier-Dupouy F, Proudhon H, Renault P O, Thilly L, et al. Multiscale modeling of the elasto-plastic behavior of architectured and nanostructured Cu–Nb composite wires and comparison with neutron diffraction experiments. *Int J Plasticity* **122**: 1–30 (2019)
[88] Gu T, Stopka K S, Xu C, McDowell D L. Modeling the statistical distribution of fatigue crack formation lifetime in large volumes of polycrystalline microstructures. *Acta Mater* **247**: 118715 (2023)
[89] Gu T, Wang B L, Zhu T, Castelluccio G M, McDowell D L. Two-way coupled modeling of dislocation substructure sensitive crystal plasticity and hydrogen diffusion at the crack tip of FCC single crystals. *Int J Solids Struct* **306**: 113072 (2025)

Ming Liu received his Ph.D. degree in materials science and engineering from the University of Kentucky, USA, in 2012. He was a postdoctorate researcher at the Centre of Materials, Mines Paris Tech France, France, and Washington State University, USA, in 2013 and 2014, respectively. He joined the School of Mechanical Engineering and Automation, Fuzhou University, China, in 2015 and was directly promoted to professor and doctoral supervisor under the Fujian Provincial Minjiang Scholar Program. He was included in Stanford University's 2023 list of the world's top 2% scientists and has been working as a postdoctoral researcher at Macau University of Science and Technology, China, since 2024. His research focuses on micromechanical testing and analysis via indentation and scratch methods, as well as finite element modeling.

Zhitong Xu obtained his master degree in solid mechanics and his bachelor degree in mechanical design, manufacturing and automation in 2021 and 2018, respectively, from the School of Mechanical Engineering and Automation, Fuzhou University, China. His research focused on characterizing the mechanical properties of solids via instrumented indentation and scratch methods.

Noraphat Yuktanan is pursuing his research master degree at Institute of Polytechnic Science and Aeronautics (IPSA), France. He received his Bachelor of Engineering degree from Chulalongkorn University. His research interests include aerospace propulsion, computational mechanics, and numerical simulation.

Tang Gu has been an assistant professor at IPSA, France, since 2022. He received his Ph.D. degree in mechanics of materials from MINES Paris – PSL & ENSAM, France, in 2017 and conducted postdoctoral research at the Georgia Institute of Technology from 2017 to 2021. His research interests include crystal plasticity, multiscale and multiphysics modeling, and AI-assisted computational mechanics.

Guangan Zhang received his Ph.D. degree from Lanzhou University, China, in 2006. He is currently a professor at the State Key Laboratory of Solid Lubrication, Lanzhou Institute of Chemical Physics, Chinese Academy of Sciences, China. He has successfully developed a series of solid lubrication coatings, such as diamond-like carbon, molybdenum disulfide, and metal nitride coatings, and has served as a member of the Surface Engineering Branch of the China Mechanical Engineering Society. His research interests are the promotion and application of physical vapor deposition (PVD) and plasma-enhanced chemical vapor deposition (PECVD) technology on mechanical moving parts.

Jinyang Jiang, Ph.D., a chief professor at Southeast University, China, has long been dedicated to research and technologies related to durability design and enhancement of structural concrete. He has deciphered the time-varying characteristics of structural concretes of nanomicro-mesoscale and macroscale structures, established models for predicting the mechanical and durability properties of concrete, and pioneered theoretical and technical methods for enhancing concrete infrastructure in harsh environments. He has published over 200 SCI/EI articles and held over 40 patents and copyrights.

Fuqian Yang, Ph.D., is a full professor in the materials program at the University of Kentucky, USA. His research specializes in diffusion-induced stress and multiscale micromechanical testing and characterization techniques, including nanoindentation, atomic force microscopy, microindentation, and dynamic mechanical analysis. He is also actively involved in the synthesis of nanomaterials.

Rui Liang is an assistant professor in the Department of Engineering Science, Faculty of Innovation Engineering at Macau University of Science and Technology. She received her Ph.D. degree in civil and environmental engineering, The Hong Kong University of Science and Technology, Hong Kong, China, in 2018. Her research interests focus mainly on organic/inorganic composites, high-strength lightweight concrete, and polymer-modified cementitious materials.